Solidification of the Lennard-Jones fluid near a wall in thermohydrodynamic lubrication

Kouki Nakamura, Ryo Ookawa, and Shugo Yasuda [*]

Graduate School of Simulation Studies, University of Hyogo, Kobe 650-0047, Japan

We investigate the thermohydrodynamic lubrication of the Lennard-Jones (LJ) fluid in plain wall channels by using a molecular-dynamics simulation. It is found that the LJ fluid solidifies near the wall when the viscous heating of the LJ fluid in the bulk regime is sufficiently large. The thickness of the solidified layer increases with the channel width. Thus, a long-range-ordered crystal-like structure forms near the wall in high-speed lubrication when the channel width is large. The mechanism of this counterintuitive solidification is investigated from both macroscopic and microscopic points of view. It is elucidated that the LJ molecules are densely confined in the vicinity of the wall due to the macroscopic mass and heat transport in the bulk regime. In this densely confined regime, the fluid molecules form a crystal-like structure, which is similar to that of the wall molecules, via direct molecular interaction. Band formation is also observed in the solidified region when the channel width is sufficiently large.

I. INTRODUCTION

The molecular-dynamics (MD) study of nanoscale flows is a very active research field due to the development of the micro- and nanotechnologies. It has been clarified both experimentally and theoretically that particular flow behavior that cannot be described by the hydrodynamic equation, i.e., the Navier-Stokes equation, such as slip flows at boundaries [1–3] and phase transition in molecularly confined channels [4–8], are significant among nanoscale flows. On the other hand, it is usually considered that that particular flow behavior is less significant when the channel size is much larger than the molecular scale; for example, over several hundred nanometers, and that the flow behavior in plain wall channels is well described by classic hydrodynamic theory such as the Reynolds approximation [9].

However, recently, we reported in a proceedings paper [10] that solidification may occur near the plain wall in high-speed lubrication even if the channel size is much larger than the molecular scale. Interestingly, we also found that solidification only occurs when the bulk fluid is highly heated due to the viscous dissipation in high-speed shear flows.

In this paper, we aim to unveil the mechanism of the counterintuitive solidification from both microscopic and macroscopic points of view. We carry out large-scale MD simulations of the Lennard-Jones (LJ) fluid in high-speed lubrication while changing various physical parameters such as the channel width, wall speed, wall temperature, fluid density, and lattice structure of the wall molecules. We focus on the thermohydrodynamic coupling of mass, momentum, and energy transfer in the bulk regime and clarify the solidification mechanism in relation to macroscopic thermohydrodynamic coupling.

MD simulations of thermohydrodynamic lubrication in molecularly thin layers between plane walls, where the channel width is typically only several tens of nanometers, were previously investigated in the literature [11–18]. These studies clarified the distinctive features of nanoscale flows due to the direct interaction between the fluid and the wall molecules at the interface, such as the slip flow and density layering at the boundaries.

For example, in Ref. [12], the effects of viscous heating on the transport properties in planar Couette flows between thermal walls were investigated, and a qualitatively different shear-rate dependence of transport coefficients with and without viscous heating was clarified. The effects of the fluid-wall interaction on the velocity slip and temperature jump at wall boundaries were also investigated [14–16]; e.g., in Ref. [15], it was clarified that the Navier-Stokes equation can well describe the flow behavior when a fluid-wall interaction was sufficiently large, while in Ref. [16], it was demonstrated that the velocity slip and temperature jump became significant when the fluid-wall interaction was small. A temperature profile qualitatively different from conventional fluid dynamics was also discovered in planar Poiseuille flows in Ref. [13] and was discussed in detail in Ref. [17].

Apart from that particular flow behavior occurring only in molecularly thin layers, this study considers the case where the channel width is much larger than the molecular scale; for example, over several hundred nanometers: the direct interaction between the fluid and the wall molecules is only restricted in close vicinity of the wall, and macroscopic transport becomes significant in the bulk-fluid regime.

We describe the problem and simulation model considered in this study in Sec. II. The simulation results are given in Sec. III, where the counterintuitive solidification is also revealed. In Sec. IV, the solidification mechanism is discussed from both macroscopic and microscopic points of view. Finally, we provide concluding remarks in Sec. V.
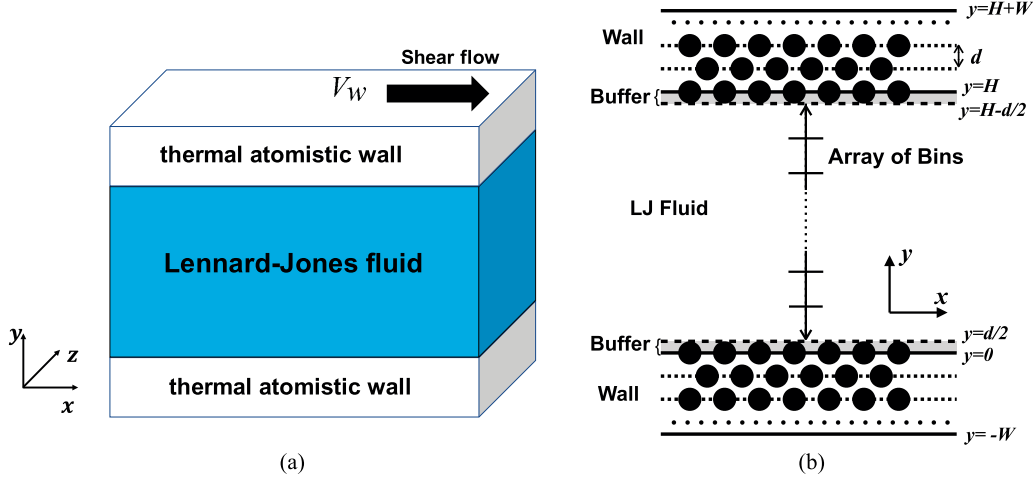
———————
[*]yasuda@sim.u-hyogo.ac.jp

FIG. 1. (a) Schematic diagram of problem and (b) the setting of the bins for the calculation of local macroscopic quantities. In panel (a), the LJ fluid is sandwiched between atomistic walls kept at a constant temperature T^w. Boundary-driven shear flows and force-driven flows are considered. The x axis is parallel to the flow direction, and the y axis points in the direction perpendicular to the parallel walls. In the x direction, periodic boundary conditions are considered. In panel (b), the width of the channel, except for thin layers on the boundaries between the fluid and the channel walls, is uniformly divided into 20 bins, and the local macroscopic quantities are calculated in each bin. The thickness of each thin layer is $\frac{d}{2}$, where d is the size of the gap between layers of the fcc lattice structure.

II. PROBLEM AND SIMULATION MODEL

The LJ fluid between parallel plain walls is considered [see Fig. 1(a)]. The fluid domain extends $0 < y < H$, and the wall domains extend $-W \leqslant y \leqslant 0$ (the lower wall) and $H \leqslant y \leqslant H + W$ (the upper wall). Both the fluid and the walls are composed of LJ particles that interact with each other via the LJ potential:

$$U(r) = \begin{cases} 4\varepsilon\left[\left(\frac{\sigma}{r}\right)^{12} - \left(\frac{\sigma}{r}\right)^6\right] & (0 < r < r_c) \\ 0 & (r_c \leqslant r). \end{cases} \quad (1)$$

Here, r_c is the cutoff parameter, and ε and σ are the units of energy and length of the LJ particles, respectively.

The wall particles are connected to the face-centered cubic (fcc) lattice structure (whose lattice nodes are denoted by $\{r_i^w\}$) by a spring potential, and the temperature of the wall particles is kept at a constant value of T^w by the Langevin thermostat algorithm [19–21]. On the other hand, the temperature of the fluid domain is not artificially controlled by any thermostat algorithm but varies autonomously according to the mass, momentum, and heat transfer between the thermal walls.

Thus, the dynamics of the LJ particles in the fluid domain [i.e., $r_{y_i} \in (0, H)$] are described by

$$m\ddot{r}_i(t) = -\sum_j \frac{\partial U(|r_{ij}|)}{\partial r_{ij}} \quad (2)$$

while, for the wall particles (i.e., $r_{y_i} \in [-W, 0] \cup [H, H + W]$), the dynamics are described by

$$m\ddot{r}_i(t) = -\sum_j \frac{\partial U(|r_{ij}|)}{\partial r_{ij}} - k_s(r_i - r_i^w) - \gamma\dot{r}_i + R(t), \quad (3)$$

where $R_\alpha(t)$ ($\alpha = x, y, z$) is white Gaussian noise that satisfies

$$\langle R_\alpha(t)R_\beta(t - s)\rangle = 2mk_BT^w\gamma\delta_{\alpha\beta}\delta(s). \quad (4)$$

Here, r_i represents the position of the ith particle, r_{ij} is defined as $r_{ij} = r_i - r_j$, m is the mass of a LJ particle, k_s is the spring constant, γ is the damping coefficient, k_B is the Boltzmann constant, and the summation $\sum_j$ applies to both the fluid and wall particles. Note that the temperature of the upper wall is controlled by the Gaussian noise only in the y and z directions.

In this study, we only consider the case where the wall and fluid particles are the same in size and mass. The cutoff length $r_c = 2.8$, the spring constant $k_s = 10$ and the damping coefficient $\gamma = 0.1$ are fixed. Hereafter, we express quantities in units of mass m, energy ε, length σ, and time $\tau = \sqrt{m\sigma^2/\varepsilon}$.

The LJ fluid is initially in a uniform liquid state with a density ρ_0 and a temperature T_0. This initial state of the LJ fluid is produced by a long-time (i.e., 2×10^7 time steps) quiescent MD simulation of the system shown in Fig. 1(a). The radial distribution function (RDF) of the initial liquid state is shown in Fig. 4(b).

At time $t = 0$, the upper wall starts to move from left to right with a speed V_w, and the wall-driven shear flow is produced in the fluid domain between the walls.

III. RESULTS

In this section, we only consider the initial density $\rho_0 = 0.844$ and initial temperature $T_0 = 0.722$, which is near the triple point of the LJ potential (the effects of the initial state will be discussed in the next section). The channel width varies as $H = 168, 252, 336, 420,$ and 504, whereas the side lengths of the simulation box $L_x = L_z = 16.8$ and the thickness of the wall $W \simeq 4.1$ are fixed. The speed of the upper wall also varies as $V_w = 1.0, 1.5, 1.75, 2.0, 2.5,$ and 3.0 for each channel width H.

The MD simulations are performed using the LAMMPS software package [22,23], in which Eq. (2) is time-integrated via the velocity Verlet method with a time-step size of $\Delta t = 0.005$.

The width of the channel except the thin buffer layers along the boundaries [see Fig. 1(b)], i.e., $\frac{d}{2} < y < H - \frac{d}{2}$, is uniformly divided into 20 bins, and in each bin, the local macroscopic quantities, i.e., the density ρ, the flow velocity u_x, the temperature T, and the stress $p_{\alpha\beta}$, are calculated via the following equations:

$$\rho(l) = \frac{1}{|V_{\text{bin}}^l|} \int_{\boldsymbol{r} \in V_{\text{bin}}^l} \sum_i \delta(\boldsymbol{r} - \boldsymbol{r}_i) d\boldsymbol{r}, \tag{5}$$

$$\rho(l) u_x(l) = \frac{1}{|V_{\text{bin}}^l|} \int_{\boldsymbol{r} \in V_{\text{bin}}^l} \sum_i \dot{r}_{x\,i} \, \delta(\boldsymbol{r} - \boldsymbol{r}_i) d\boldsymbol{r}, \tag{6}$$

$$\rho(l) T(l) = \frac{1}{3|V_{\text{bin}}^l|} \int_{\boldsymbol{r} \in V_{\text{bin}}^l} \sum_i [\dot{\boldsymbol{r}}_i - u_x(l)\delta_{x\alpha}]^2 \delta(\boldsymbol{r} - \boldsymbol{r}_i) d\boldsymbol{r}, \tag{7}$$

$$p_{\alpha\beta}(l) = \frac{1}{|V_{\text{bin}}^l|} \int_{\boldsymbol{r} \in V_{\text{bin}}^l} \sum_i \{[\dot{r}_{\alpha\,i} - u_x(l)\delta_{x\alpha}]\dot{r}_{\beta\,i} + r_{\alpha\,i} f_{\beta\,i}\}$$
$$\times \delta(\boldsymbol{r} - \boldsymbol{r}_i) d\boldsymbol{r}, \tag{8}$$

where the summation $\sum_i$ is taken over all the molecules and V_{bin}^l and $|V_{\text{bin}}^l|$ represent the region of the lth bin and the volume of the local bin, respectively. On the right-hand side of Eq. (8), $\boldsymbol{f}_i$ is the force applied to the ith molecule due to the interaction among the ambient molecules, i.e., the right-hand side of Eq. (2).

The local quantities are also time-averaged in the stationary state after a long time t_0 has passed (i.e., $t_0 = 4 \times 10^7 \Delta t$), where the instantaneous quantities are sampled every 10 time steps in the interval $t = [t_0, \, t_0 + 10^5 \Delta t]$ (i.e., 10^4 samples are averaged for each local quantity). The standard deviations of the instantaneous local macroscopic quantities shown in Fig. 2 are at most 0.012 for the velocity u_x, 0.013 for the temperature T, 0.0026 for the density ρ, 0.075 for the shear stress p_{xy}, and 0.12 for the normal stress p_{yy}. The local viscosity is calculated from the time-averaged quantities as $\mu = p_{xy}/(du_x/dy)$.

In this section, we mainly show the results for $H = 504$. The results for other channel widths are given in Ref. [24].

A. Distribution of macroscopic quantities

Figure 2 shows the spatial distributions of the local macroscopic quantities (i.e., velocity, temperature, density, and stress) and local viscosity for different wall speeds V_w. It is seen that the normal and shear stresses, p_{yy} and p_{xy}, are uniform between the upper and lower walls for all cases. This confirms that the local stresses are balanced so that the flow velocity is in the stationary state.

The other macroscopic quantities vary spatially between the walls. The temperature increases in the middle region due to viscous heating, while it remains close to the wall temperature near the walls. By contrast, the local density decreases in the middle but increases near the walls.

Remarkably, for $V_w = 2.5$ and 3, we can observe significant jumps in local density and local viscosity near the walls. Related to the rapid increase in the local viscosity in the vicinity of the wall, the velocity profile becomes nonlinear; i.e., the velocity gradient becomes much smaller near the wall than in the middle of the channel.

In the following text, we focus on the peculiar behavior observed in the vicinity of the wall when the wall speed is large.
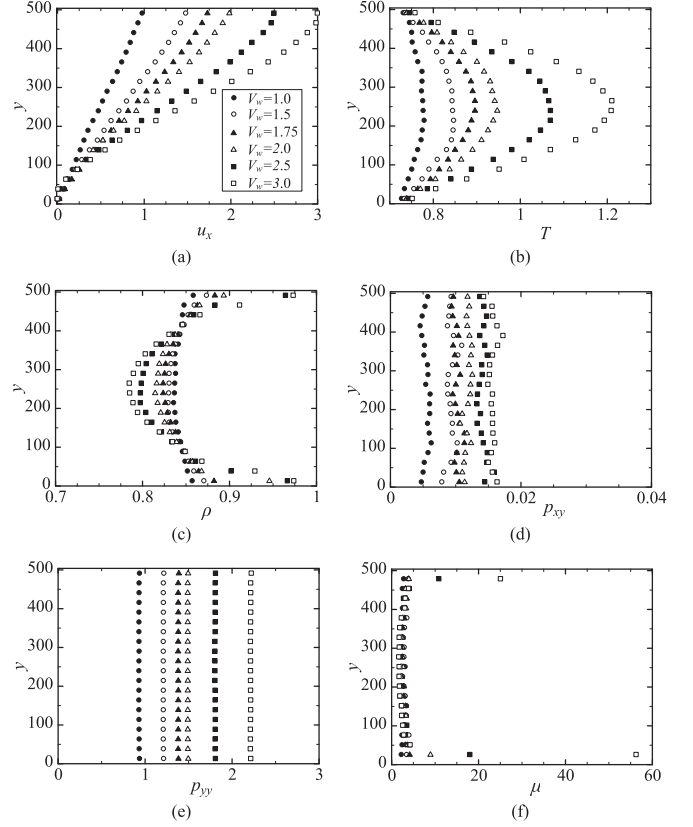

FIG. 2. The spatial distributions of the macroscopic quantities, i.e., (a) velocity u_x, (b) temperature T, (c) density ρ, (d) shear stress p_{xy}, (e) normal stress p_{yy}, and (f) local viscosity μ, for different wall velocities V_w in the channel where $H = 504$.

B. Solidification

Figure 3 shows snapshots of the local distributions of molecules in the lower, middle, and upper regions at two different time steps. From the motions of tracer particles, we can distinguish the different diffusive behavior of local molecules between in the vicinity of the walls and in the middle of the channel. It is clearly seen that the tracer molecules in the vicinity of the walls do not diffuse in the lateral direction (y axis) but rather form a long-range-ordered crystal-like structure, which is similar to that of the wall molecules. On the other hand, the molecules in the middle region diffuse in the lateral direction, as is observed in the fluid phase.

We can also observe the bands in the solidified layer in Fig. 3, where the bands run diagonally right upward near the upper wall. However, the direction of the band is not always diagonally right upward; instead, it may be the opposite direction or even appear in the yz cross section. See Fig. 5 in the Supplemental Material [24]. This observation indicates that band formation is not directly related to the flow velocity but rather to the compression of molecules from the bulk region toward the walls.

It is also seen from the supplementary figure [24] that the solidification of the LJ fluid near the wall occurs only when the wall speed is sufficiently large, e.g., $V_w \geqslant 2$. When the wall speed is small, we observe only a thin absorption layer
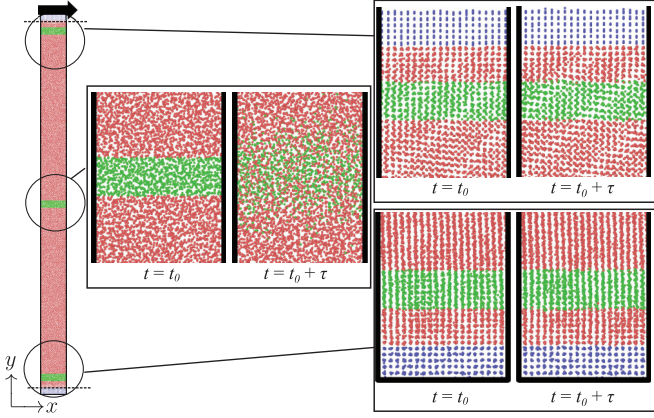
FIG. 3. Snapshots of molecules in the lower, middle, and upper regions at two different time steps for $H = 504$ and $V_w = 3.0$. Three-dimensional particle distributions extended in the depth direction $0 < z < L_z$ are projected onto the x-y plane. Thus, the LJ particles, which align in the depth direction of the fcc lattice, overlap and form a regular square lattice in the projection map. The motion of (green-colored) tracer particles after $\tau = 10\,000$ time steps have passed is monitored. In the figures, the diameter of each tracer particle is set to 0.3σ.

of molecules on the surface of the wall. The thickness of the absorption layer is only the length of a few molecules.

We also calculate the local RDF in the lth bin by

$$g^l(r) = \left\langle \frac{n_i(r)}{4\pi r^2 dr \rho_0} \right\rangle_l, \tag{9}$$

where $n^i(r)$ counts the number of molecules within the distance $[r,\ r + dr]$ from the ith molecule in the lth bin and $\langle\ \rangle_l$ represents the ensemble average over all the molecules contained in the local bin. Figure 4 shows the local RDFs of the molecules in the upper, lower, and middle regions. It is clearly seen that the RDFs near the walls have similar peak profiles to those of the fcc lattice structure of the wall, while the RDF in the middle region remains in the initial fluid state. This result also quantitatively confirms that the solidification occurs near
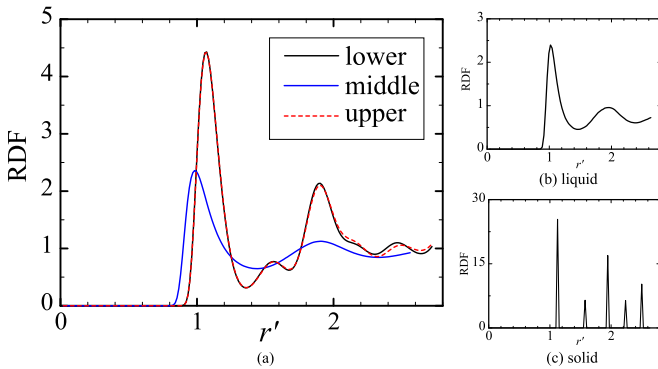

FIG. 4. Panel (a) shows the RDFs of the molecules in the upper, middle, and lower bins at time $t = t_0$. Panels (b) and (c) show the RDFs for the initial liquid state near the triple point and for the fcc lattice structure of the wall, respectively. The horizontal axis is scaled as $r' = r/\rho^{-1/3}$. The channel width $H = 504$, and the wall speed $V_w = 3.0$.
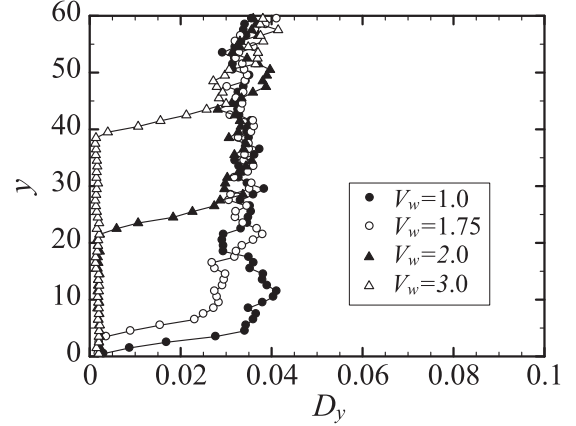

FIG. 5. The spatial distributions of the local lateral diffusion coefficient D_y defined by Eq. (10) for different plate speeds $V_w = 1.0$, 1.75, and 2.5 for the channel width $H = 504$.

the walls and that the lattice structures in the solidified layers are similar to those of the walls. In Sec. IV C, we discuss the effect of the wall structure in detail. To distinguish between the fluid and solidified phases, we measure the local lateral diffusion coefficient D_y defined by

$$D_y = \int_0^\infty \left\langle \left\langle v_y^i(t + \tau) v_y^i(\tau) \right\rangle_\tau \right\rangle_l dt, \tag{10}$$

where v_y^i represents the lateral velocity of the ith molecules in the lth local bin and $\langle\ \rangle_\tau$ represents the ensemble average over different τ.

Figure 5 shows the spatial distributions of the local lateral diffusion coefficient for different wall speeds. It is clearly seen that the lateral diffusion coefficient D_y is negligibly small; say $D_y < 0.01$, in the solidified or absorption layer near the wall. The solidified layer with the small lateral diffusion coefficient rapidly broadens when the wall speed changes from $V_w = 1.75$ to 2.0. We summarize the results of the solidification under different parameters in Fig. 6, in which a diagram of the solidification vs the channel width H and the square of the wall speed V_w^2 is shown. In the figure, the thickness of the solidified layer l_S, which is defined by the thickness of the layer where the local lateral diffusion coefficient is smaller than 0.01, i.e., $D_y < 0.01$, is indicated by the color legend. The square symbols $\square$ represent the results obtained when the solidified layer extends far beyond the molecular size, i.e., $l_S > 10$. It is clearly seen that long-range-ordered crystal structures are observed only when the wall speed is sufficiently large, e.g., $V_w \geqslant 2$. See also the figures in the Supplemental Material [24]. In the high-speed regime, $V_w \geqslant 2$, the thickness of the solid layer l_S proportionally increases with the channel width H (see Fig. 7). The mechanism underlying these observations will be discussed in the next section.

Incidentally, in Fig. 6, the square of the wall speed, V_w^2, is used as the horizontal axis rather than the wall speed itself. This is because V_w^2 represents the amplitude of the viscous heating relative to the thermal conduction in macroscopic energy transport, i.e.,

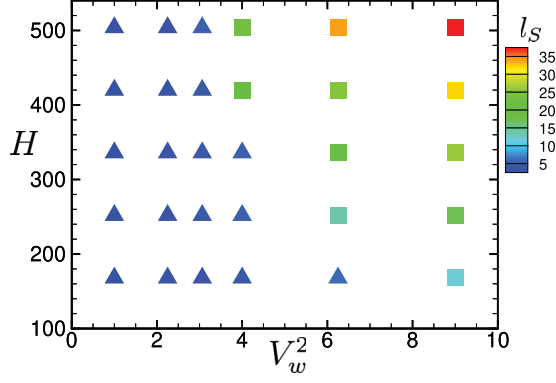$$\frac{\mu V_w^2/H^2}{\lambda \Delta T/H^2} \propto V_w^2, \tag{11}$$

FIG. 6. Diagram of the phase states near the wall vs the channel width H and the square of the wall speed, V_w^2. The square symbols show the results obtained when the thickness of the solidified layer l_S, which is defined by the thickness of the layer whose lateral diffusion coefficient is as small as $D_y < 0.01$, is $l_S > 10$. The solid line shows the critical line for the solidification obtained by a crude theoretical estimate, and the dashed line shows the asymptotic limit of the critical line.

where λ is the thermal conductivity and ΔT is a characteristic temperature rise.

IV. DISCUSSION

A. Macroscopic explanation

In this section, we consider the mechanism of the solidification from a macroscopic point of view. We suppose a Newtonian fluid with a constant viscosity μ and the Fourier law of heat conduction with a constant thermal conductivity λ. We also introduce the normalized coordinate $\hat{y} = y/H$, which is relevant to the hydrodynamic analysis. In the following part of this section, we consider only the stationary state. Then, the spatial distribution of temperature is described by

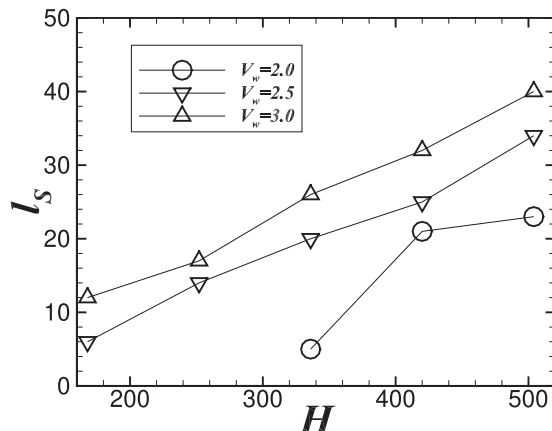$$-\frac{d^2 T}{d\hat{y}^2} = \frac{\mu}{\lambda} V_w^2, \tag{12}$$

FIG. 7. The thickness of the solidified layer l_S vs the channel width H for large wall speeds, i.e., $V_w = 2.0$, 2.5, and 3.0.
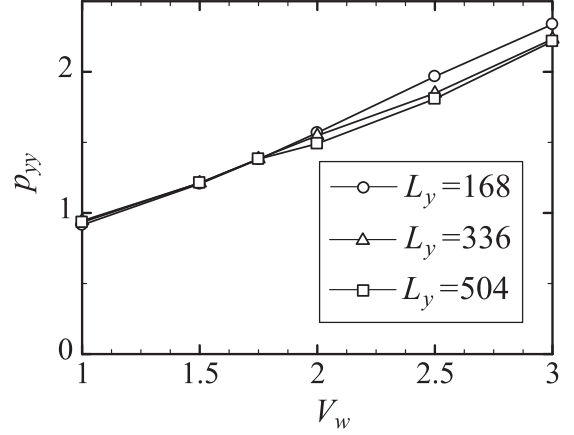

FIG. 8. The bulk pressure p_{yy} vs wall speed V_w for various channel widths H.

with the boundary condition $T = T_w$ at $\hat{y} = 0$ and 1. The solution to the above equation is explicitly calculated as

$$T(\hat{y}) = 4\Delta T \hat{y}(1 - \hat{y}) + T_w, \tag{13}$$

where $\Delta T = \mu V_w^2/8\lambda$ is the difference in temperatures between the region at the wall and the region in the middle of the channel.

The mass conservation is written as

$$\int_0^1 \rho(\hat{y})d\hat{y} = \rho_0, \tag{14}$$

where ρ_0 is the initial density of the LJ fluid. We can also easily obtain from the momentum balance equation that the bulk pressure is spatially uniform in the stationary state because of the continuity condition $\frac{\partial v_y}{\partial \hat{y}} = 0$.

We suppose that the equation of state $\rho = \mathcal{F}(p, T)$ holds at the local fluid elements even in the steady shear flow and satisfies the conditions $(\frac{\partial \mathcal{F}}{\partial T})_p < 0$ and $(\frac{\partial \mathcal{F}}{\partial p})_T > 0$. Then, the bulk pressure p is determined from the equation

$$\int_0^1 \mathcal{F}(p, T(\hat{y}))d\hat{y} = \rho_0. \tag{15}$$

This indicates that the bulk pressure does not depend on the channel width H but depends only on the wall speed V_w when the initial states ρ_0 and T_w are fixed since $T(\hat{y})$ does not depend on the channel width H in Eq. (13).

The dependency of the bulk pressure on the wall speed is obtained by taking the derivative of Eq. (15) against V_w, i.e.,

$$\int_0^1 \left(\frac{dp}{dV_w}\right)\left(\frac{\partial \mathcal{F}}{\partial p}\right)_p d\hat{y} + \int_0^1 \left(\frac{\partial T}{\partial V_w}\right)\left(\frac{\partial \mathcal{F}}{\partial T}\right)_T d\hat{y} = 0,$$

$$\frac{dp}{dV_w} = -\int_0^1 \left(\frac{\partial T}{\partial V_w}\right)\left(\frac{\partial \mathcal{F}}{\partial T}\right)_T d\hat{y} \Big/ \int_0^1 \left(\frac{\partial \mathcal{F}}{\partial p}\right)_T d\hat{y} > 0, \tag{16}$$

because, from Eq. (13), $\frac{\partial T}{\partial V_w} > 0$ holds at any local position $\hat{y} \in (0, 1)$. Thus, the bulk pressure monotonically increases with the wall velocity V_w. In fact, in Fig. 8, our simulation results demonstrate that the bulk pressure monotonically increases with the wall speed but is less dependent on the channel width.
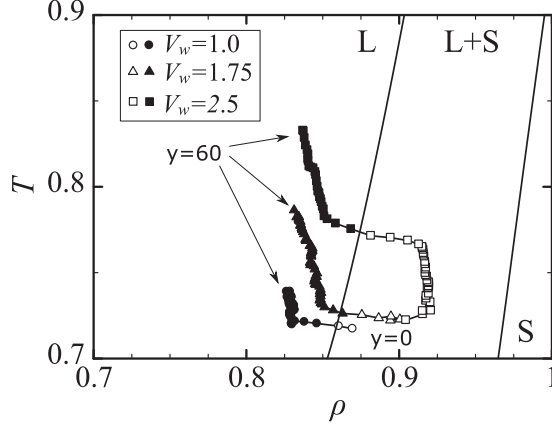
FIG. 9. The transient behavior of the local ρ-T states between the bulk regime ($y = 60$) and the surface of the wall $y = 0$ for different wall speeds, i.e., $V_w = 1.0$, 1.75, and 2.5. The initial density $\rho_0 = 0.884$, the initial temperature $T_w = 0.772$, and the channel width $H = 504$ are fixed. In the ρ-T plane, the upper left corresponds to the bulk regime, and the lower right corresponds to the vicinity of the wall. The closed marks indicate that the local lateral diffusion coefficients are smaller than 0.01, i.e., the fluid regime, and the open marks indicate that the local lateral diffusion coefficients are larger than 0.01, i.e., the solid regime. In the phase diagram, "L" represents the liquid phase; "S" represents the solid phase; and "L + S" represents the liquid-solid coexistence phase. The solidification and melting lines (the left and right solid lines, respectively) are drawn by using the formulas obtained from Ref. [25].

The local density is described by the equation of state as $\rho(\hat{y}) = \mathcal{F}(p, T(\hat{y}))$, where the bulk pressure p is spatially uniform and the temperature is described by Eq. (13). It is seen that the local density monotonically increases while approaching the wall [under the condition $(\frac{\partial \mathcal{F}}{\partial T})_p < 0$] and takes the maximum value at the wall, i.e., $\rho(\hat{y}) \nearrow \rho_w = \mathcal{F}(p, T_w)$ as $\hat{y} \to 0$ or 1. This indicates that the local density in the vicinity of the wall monotonically increases with the wall speed V_w but does not depend on the channel width H in the same way as the bulk pressure.

Thus, if we suppose that the fluid is solidified when the local density exceeds a critical density ρ^*, the solidification never occurs unless the wall velocity exceeds the critical velocity V_w^*, which satisfies $\rho^* = \mathcal{F}(p(V_w^*), T_w)$, regardless of the channel width H. This concisely explains the observation of the existence of a critical wall speed for the solidification in Fig. 6.

The reason why the thickness of the solidified layer, l_S, is proportional to the channel width H is also explained; i.e., the local density is a monotonic function of $\hat{y}$ and independent of H, so the solidified layer, where the local density is larger than the critical density, i.e., $\rho(\hat{y}) > \rho^*$, is uniquely determined by the condition $\rho(l_S/H) = \rho^*$ for a given wall velocity. Thus, the thickness of the solidified layer l_S is proportional to the channel width H.

B. Transient of the local state

Figure 9 shows the transient behavior of the local ρ-T states between the bulk ($y = 60$) and the interface of the wall

($y = 0$). Here, instead of using Eq. (5), we calculate the local density by using

$$\rho(l) = \frac{1 + \int_0^{r_c} 4\pi r^2 \rho_0 g^l(r) dr}{\frac{4}{3}\pi r_c^3}, \quad (17)$$

where the local RDF $g^l(r)$ is defined in Eq. (9). It is seen that the conditions supposed in the previous section, i.e., $(\frac{\partial \mathcal{F}}{\partial T})_p < 0$ and $(\frac{\partial \mathcal{F}}{\partial p})_T > 0$, are relevant to the simulation results and, in fact, the maximum density increases with the wall speed V_w.

The local density rapidly increases around the solidification line while approaching the wall from the bulk, and the ρ-T state enters into the liquid-solid coexistence regime in the phase diagram. For a large wall speed $V_w = 2.5$, remarkable solidification (or crystallization) is observed even in the liquid-solid coexistence regime, where the thermal expansion becomes very small, i.e., $|\frac{1}{\rho}(\frac{\partial \rho}{\partial T})_p| \ll 1$, as is usually observed in solid materials. For a small wall speed $V_w < 2$, solidification is remarkably not observed, but a thin absorption layer forms on the surface of the wall (see also Fig. 5).

These observations demonstrates that the LJ molecules in the fluid phase are confined in the vicinity of the wall due to the thermohydrodynamic coupling and that, when the density in the confined regime is close to the solidification line, the tightly confined LJ molecules are solidified via the interaction with the wall molecules. This also indicates that both the wall structure and the ρ-T state in the vicinity of the wall strongly affect the solidification near the wall.

C. Effects of the wall structure and the initial state

Thus far, we have considered the face-centered-cubic (fcc) lattice structure for the wall molecules and the initial condition of the LJ fluid near the triple point, i.e., $\rho_0 = 0.844$ and $T_0 = 0.722$. In this section, we change the wall structure and the initial condition and investigate the effects of the wall structure and the initial condition of the LJ fluid.

Figure 10 shows snapshots of the molecules composing the bottom wall (i.e., $-W < y < 0$) and those in the vicinity of the wall (i.e., $0 < y \leqslant 60$) for the channel width $H \simeq 500$ and the wall velocity $V_w = 3.0$. It is seen that solidification occurs with both the fcc and bcc structures.

Interestingly, the lattice structures of the solidified layer are different from each other. With the bcc wall, the LJ molecules in the solidified layer also create the bcc lattice structure, although it is known that the fcc structure appears during the crystallization of the LJ molecules in the equilibrium state. The thickness of the solidified layer is also affected to the wall structure; i.e., the solidified layer for the bcc wall is thinner than that for the fcc wall. Figure 11 shows the transient behavior of local ρ-T states from the bulk regime to the surface of the wall for three different initial states of the LJ fluid. If the initial state is close to the solidification line (i.e., the square $\square$), remarkable solidification is observed in the liquid-solid coexistence regime in the phase diagram. Even if the initial state is slightly away from the solidification line (i.e., the circle $\circ$), we can observe that the solidified layer
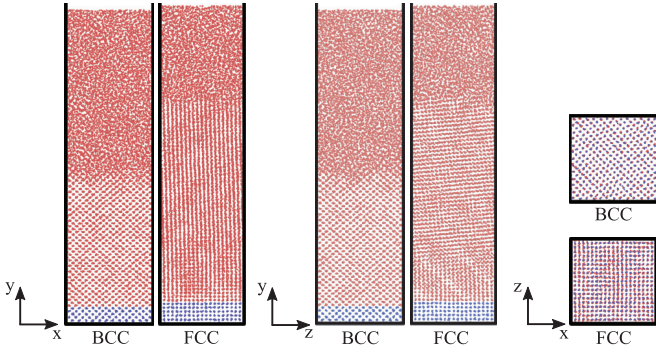
FIG. 10. Snapshots of the LJ particles in the vicinity of the bottom wall and the wall molecules for the bcc wall (in the left column) and the fcc wall (in the right column). The snapshots are shown from three different angles of view. In both the bcc and fcc structures, the channel width is $H \simeq 500$, and the wall velocity is $V_w = 3.0$. The four figures on the left side are the projections of LJ particles in the domain $[0, L_x] \times [-W, 60] \times [0, L_z]$ onto the x-y and y-z planes. The two figures on the right side are the projections of LJ particles in the domain $[0, L_x] \times [-W, 10] \times [0, L_z]$ onto the x-z plane.

forms in the vicinity of the wall. However, when the initial state is far from the solidification line (i.e., the triangle $\triangledown$), the local ρ-T state cannot approach the solidification line even in the vicinity of the wall, so solidification does not occur in the vicinity of the wall.

From these observations, we can conclude that the LJ molecules are confined in the vicinity of the wall via thermohydrodynamic transport and that when the local ρ-T state is close to the solidification line in the vicinity of the wall, the LJ molecules are solidified due to the interaction with the crystallized wall molecules.
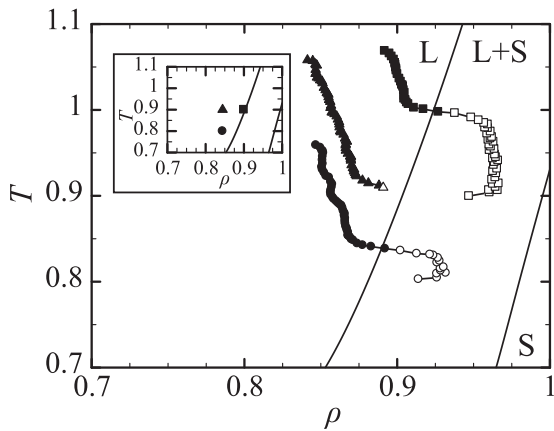

FIG. 11. The transient behavior of the local ρ-T states between the bulk regime ($y = 60$) and the surface of the wall $y = 0$ for different initial states, which are shown in the inset, i.e., $\rho_0 = 0.8442$ and $T = 0.8$ for the circle $\bigcirc$, $\rho_0 = 0.8442$ and $T = 0.9$ for the triangle $\triangle$, and $\rho_0 = 0.9$ and $T = 0.9$ for the square $\square$. The wall speed $V_w = 3.0$ and channel width $H \simeq 500$ are fixed. See also the caption in Fig. 9.
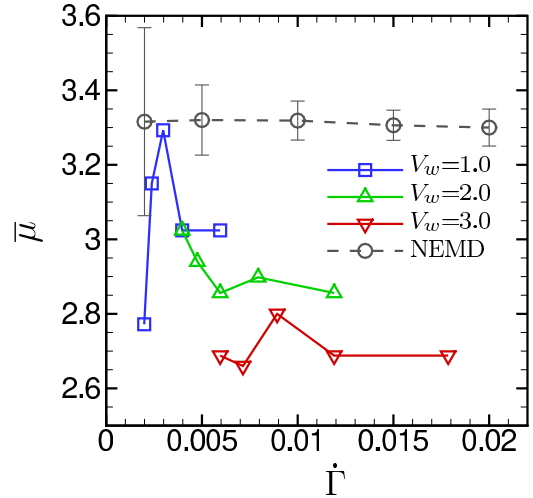

FIG. 12. The gross viscosity $\overline{\mu}$ vs the gross shear rate $\dot{\Gamma} = V_w/H$. The gross viscosity is calculated by the ratio of the spatial average of local shear stress p_{xy} to the gross shear rate, i.e., $\overline{\mu} = \frac{1}{H} \int_0^H p_{xy}(y) dy / \dot{\Gamma}$. The squares $\square$ show the results for $V_w = 1.0$; the upward triangles $\triangle$, for $V_w = 2.0$; and the downward triangles $\triangledown$, for $V_w = 3.0$. The circles $\bigcirc$ and error bars show the results obtained by a nonequilibrium MD simulation of the uniform LJ fluid with temperature $T = 0.772$ and density $\rho = 0.844$.

D. Gross viscosity

Figure 12 shows the gross rheological property of the LJ fluid in the lubrication system, where the gross viscosity $\overline{\mu}$ is defined by the ratio of the spatial average of local shear stress to the gross shear rate $\dot{\Gamma} = V_w/H$, i.e., $\overline{\mu} = \frac{1}{H} \int_0^H p_{xy}(y) dy / \dot{\Gamma}$. The viscosities of the uniform LJ fluid with temperature $T = 0.772$ and density $\rho = 0.844$ under different shear strain rates, which are calculated by a nonequilibrium molecular-dynamics (NEMD) simulation with the SLLOD algorithm [20,21], are also plotted for comparison.

The NEMD simulations were performed for 3200 LJ particles in $t = [0, 10^7 \Delta t]$, and the shear viscosity was calculated by the ratio of the time average of the shear stress to the applied shear rate. The error bars show the standard deviation of the shear viscosity calculated in a time interval of $10^5 \Delta t$. It is confirmed that the LJ fluid does not show a significant shear-rate dependence in the shear viscosity in this small shear-rate regime, although the fluctuation becomes notable when the shear rate is small; for example, $\dot{\Gamma} < 0.005$.

The gross viscosity of the lubrication system also does not show an evident shear-rate dependence when the wall velocity is fixed. However, interestingly, it shows a wall-velocity dependence; i.e., the gross viscosity tends to decrease as the wall velocity increases.

This wall-velocity dependence of the gross viscosity is relevant to the viscous heating because, as observed in Sec. IV A, the hydrodynamic analysis says that the increase in temperature and the related density profile in the lubrication system does not depend on the channel width but instead depends on only the wall velocity. Thus, this result clearly demonstrates that the viscous heating may significantly affect the gross rheological properties of the lubrication system even for the simple LJ fluid.

V. CONCLUDING REMARKS AND PERSPECTIVES

We carried out MD simulations of the thermohydrodynamic lubrication of the LJ fluid between atomistic thermal walls. A counterintuitive solidification is discovered, in which the LJ fluid is solidified near the wall only when the viscous heating generated in the bulk regime is sufficiently large. The thickness of the solidified layer increases with the channel width, so the long-range-ordered crystal structure, whose width is in the range of several tens of times greater than the molecular size, forms in the vicinity of the wall when the channel width is large. Band formation is also found in the solidified layer when the channel width is large.

Although the thermal lubrication of the LJ fluid has been studied by the molecular-dynamics simulation in many publications, the large density variation involving the long-range-ordered solidification near wall was not observed in previous studies. This is because most of the molecular-dynamics studies considered only molecularly narrow channels; when the fluid molecules are confined in molecularly narrow channels, the direct interaction between fluid and wall molecules becomes dominant throughout the channel, so that the macroscopic quantities do not vary as is described by the hydrodynamic equation. We note that, in order to investigate the phase transition behavior coupled with the macroscopic hydrodynamic transport, one needs a large-scale molecular-dynamics simulation as is carried out in the present study.

We investigated the solidification mechanism in detail from both macroscopic and microscopic points of views. It was found that the LJ molecules were confined in the vicinity of the wall via thermohydrodynamic transport and that, when the local ρ-T state in the vicinity of the wall was close to the solidification line in the phase diagram, the LJ molecules were solidified due to the interaction with the crystallized wall molecules.

This study explicitly demonstrates that, even for a simple fluid in a simple geometry with plain wall boundaries, the thermohydrodynamic coupling in high-speed lubrication may affect the gross rheological property of the lubrication system and even induce long-range-ordered crystallization near the wall.

Further investigation on more realistic systems involving the electrostatic interaction and the velocity slip and temperature jump at the fluid-wall interface may represent an important future research direction.

For example, it has been clarified in previous studies [26–28] that the thermal resistance at fluid-wall interface exponentially increases as the fluid-wall interaction ϵ_{fw} becomes smaller than the fluid-fluid interaction ϵ_{ff} such that a large temperature jump arises at the interface in a small fluid-wall interaction regime, i.e., $\epsilon_{\mathrm{fw}}/\epsilon_{\mathrm{ff}} < 1$. It was also reported in Ref. [29] that the large temperature jump caused a decrease in the local viscosity near the wall in nanoscale Poiseuille flows. In the present study, we fix the fluid-wall interaction to be the same as the fluid-fluid interaction, i.e., $\epsilon_{\mathrm{fw}}/\epsilon_{\mathrm{ff}} = 1$. However, the results in the previous studies indicate that solidification near the wall may be hindered due to a large temperature jump at the interface when the fluid-wall interaction is small.

The slip velocity at the interface may also affect the solidification. It was reported in Ref. [30] that the interfacial friction between the fluid and wall caused fluid heating in nanoscale Poiseuille flows. Furthermore, the interfacial friction becomes more dominant than the internal friction (i.e., the viscous heating) in the bulk regime when the external driving force overtakes the fluid-wall interaction force. In the present study, the velocity slip at the boundary is negligibly small because both the fluid-wall interaction and the channel width are sufficiently large, so only the interfacial friction affects the fluid heating. The effect of the interfacial friction on solidification near the wall also represents interesting future research.

[1] Y. Zhu and S. Granick, Limits of the Hydrodynamic No-Slip Boundary Condition, Phys. Rev. Lett. **88**, 106102 (2002).

[2] D. C. Tretheway and C. D. Meinhart, Apparent fluid slip at hydrophobic microchannel walls, Phys. Fluids **14**, L9 (2003).

[3] G. E. Karniadakis, A. Beskok, and N. Aluru, *Microflows and Nanoflows: Fundamentals and Simulation* (Springer, New York, 2005).

[4] J. Klein and E. Kumacheva, Confinement-induced phase transitions in simple liquids, Science **269**, 816 (1995).

[5] J. Klein and E. Kumacheva, Simple liquids confined to molecularly thin layers. I. Confinement-induced liquid-to-solid phase transitions, J. Chem. Phys. **108**, 6996 (1998).

[6] C. Alba-Simionesco, B. Coasne, G. Dosseh, G. Dudziak, K. E. Gubbins, R. Radhakrishnan, and M. Sliwinska-Bartkowiak, Effects of confinement on freezing and melting, J. Phys.: Condens. Matter **18**, R15 (2006).

[7] S. Granick, Motions and relaxations of confined liquids, Science **253**, 1374 (1991).

[8] A. L. Demirel and S. Granick, Glasslike Transition of a Confined Simple Fluid, Phys. Rev. Lett. **77**, 2261 (1996).

[9] G. K. Batchelor, *An Introduction to Fluid Dynamics* (Cambridge University Press, New York, 2000).

[10] S. Yasuda and R. Ookawa, Solidification of a simple liquid near wall in high-speed shear flows, J. Phys.: Conf. Ser. **1136**, 012027 (2018).

[11] B. D. Todd, Denis J. Evans, and Peter J. Daivis, Pressure tensor for inhomogeneous fluids, Phys. Rev. E **52**, 1627 (1995).

[12] R. Khare, J. de Pablo, and A. Yethiraj, Molecular simulation and continuum mechanics study of simple fluids in non-isothermal planar Couette flows, J. Chem. Phys. **107**, 2589 (1997).

[13] B. D. Todd and D. J. Evans, Temperature profile for Poiseuille flow, Phys. Rev. E **55**, 2800 (1997).

[14] A. Jabbarzadeh, J. D. Atkinson, and R. I. Tanner, Wall slip in the molecular dynamics simulation of thin films of hexadecane, J. Chem. Phys. **110**, 2612 (1999).

[15] J. S. Hansen and J. T. Ottesen, Molecular dynamics simulations of oscillatory flows in microfluidic channels, Microfluid. Nanofluid. **2**, 301 (2006).

[16] B. H. Kim, A. Beskok, and T. Cagin, Viscous heating in nanoscale shear driven liquid flows, Microfluid. Nanofluid. **9**, 31 (2010).

[17] J. Ghorbanian and A. Beskok, Temperature profiles and heat fluxes observed in molecular dynamics simulations of force-driven liquid flows, Phys. Chem. Chem. Phys. **19**, 10317 (2017).

[18] M. Priya and Y. Rabin, Molecular dynamics simulations of shear-induced thermophoresis and non-Newtonian flow in compressible fluids, arXiv:1703.10461.

[19] K. P. Travis and D. J. Evans, Molecular spin in a fluid undergoing Poiseuille flow, Phys. Rev. E **55**, 1566 (1997).

[20] M. P. Allen and D. J. Tildesley, *Computer Simulation of Liquids* (Oxford University Press, New York, 1989).

[21] D. J. Evans and G. Morris, *Statistical Mechanics of Nonequilibrium Liquids* (Cambridge University Press, New York, 2008).

[22] S. Plimpton, Fast parallel algorithms for short-range molecular dynamics, J. Comput. Phys. **117**, 1 (1995).

[23] http://lammps.sandia.gov

[24] See Supplemental Material at http://link.aps.org/supplemental/10.1103/PhysRevE.100.033109 for the spatial distributions of macroscopic quantities and the snapshots of the molecular distributions near the wall for different simulation parameters.

[25] M. A. van der Hoef, Free energy of the Lennard-Jones solid, J. Chem. Phys. **113**, 8142 (2010).

[26] L. Xue and P. Keblinski, Two regimes of thermal resistance at a liquid-solid interface, J. Chem. Phys. **118**, 337 (2003).

[27] J. L. Barrat and F. Chiaruttini, Kapitza resistance at the liquid-solid interface, Mol. Phys. **101**, 1605 (2003).

[28] B. H. Kim, A. Beskok, and T. Cagin, Molecular dynamics simulations of thermal resistance at the liquid-solid interface, J. Chem. Phys. **129**, 174701 (2008).

[29] F. Faraji, A. Rajabpour, and F. Kowsary, Temperature profile for nanoscale Poiseuille flow: a multiscale study, J. Mech. Sci. Technol. **30**, 803 (2016).

[30] Z. Li, Surface effects on friction-induced fluid heating in nanochannel flows, Phys. Rev. E **79**, 026312 (2009).